Topological states protected by hidden symmetry

Malte Röntgen [1,2,*,†] Xuelong Chen (陈学龙) [3,*] Wenlong Gao (高文龙) [3,‡] Maxim Pyzh,[1] Peter Schmelcher,[1,4]
Vincent Pagneux,[2] Vassos Achilleos,[2] and Antonin Coutant[5,§]

[1]*Zentrum für Optische Quantentechnologien, Universität Hamburg, Luruper Chaussee 149, 22761 Hamburg, Germany*
[2]*Laboratoire d'Acoustique de l'Université du Mans, Unite Mixte de Recherche 6613, Centre National de la Recherche Scientifique,
Avenue O. Messiaen, F-72085 Le Mans Cedex 9, France*
[3]*Eastern Institute for Advanced Study, Eastern Institute of Technology, Ningbo, Zhejiang 315200, People's Republic of China*
[4]*The Hamburg Centre for Ultrafast Imaging, Universität Hamburg, Luruper Chaussee 149, 22761 Hamburg, Germany*
[5]*Aix Marseille University, Centre National de la Recherche Scientifique, Centrale Marseille, LMA UMR 7031, Marseille, France*

Symmetries play a paramount role in many aspects of topological physics. A particularly illuminating example is the Su-Schrieffer-Heeger (SSH) chain, whose reflection and chiral symmetry endow the quantization of the Zak phase and winding number, subsequently guaranteeing the existence of topological edge states. Here, we harness recent graph-theoretical results to construct families of setups whose unit cells feature neither of these symmetries, but instead a so-called latent or hidden reflection symmetry. This causes the isospectral reduction—akin to an effective Hamiltonian—of the resulting lattice to resemble an SSH model. These latent SSH models exhibit features such as multiple topological transitions, edge states, a quantized Zak phase, and, counterintuitively, immunity to orientational disorder. We confirm our findings through electric circuit experiments, where the topological edge states can be directly observed. Serving as a first proof of principle, our paper demonstrates the wealth and generality of a stroboscopic point of view, taking advantage of hidden properties such as symmetries.

I. INTRODUCTION

In the past years, topological insulators have become a main research focus of condensed matter and wave physics. A prototypical model of a one-dimensional topological insulator is the Su-Schrieffer-Heeger (SSH) chain [1]. The SSH chain hosts topological edge states, which can be understood from the quantization of the Zak phase due to the unit cell mirror symmetry. Alternatively, these topological states can be seen to be protected by chiral symmetry and characterized by the winding number topological invariant [2].

The importance of the SSH chain as a simple and prototypical topological model is reflected in the large number of physical realizations, which include acoustic [3,4], photonic [5] or nanomechanical [6] systems, as well as electric circuits [7]. Furthermore, the original SSH model has been extended in different ways, for instance, by adding more sites to the unit cell [8–10], by adding long-range couplings [11], or by converting the unit cell to a fractal [12]. The SSH model has also been generalized to higher dimensions [13,14].

In this paper, we propose a different class of extensions. Relying on recent advances in graph theory, we propose a class of models whose unit cells feature neither a chiral symmetry nor a reflection symmetry. Instead, they are designed to possess a hidden (so-called latent [15]) symmetry. In the past few years, latent symmetries have been used for a variety of purposes, including the generation of lattice systems with perfectly flat bands [16,17], the explanation of accidental degeneracies in eigenvalue spectra [18], the design of asymmetric waveguide networks with broadband equireflectionality [19–21], or the realization of stable so-called exceptional chains in non-Hermitian systems [22]. An introduction into latent symmetry is given in Ref. [23]. As we show, the effective Hamiltonian of models with latently symmetric unit cells is closely related to the classic SSH model.

In the following, we introduce the concept of such *latent SSH* models, analyze their properties, and show how large families of them can be constructed. Furthermore, we experimentally verify our predictions in electric circuit networks.

II. THEORY

A. Topology through latent symmetry

Our main idea is to design topological lattices by relying on unit cells that feature neither a mirror symmetry nor a chiral symmetry, but a hidden mirror symmetry. Two such asymmetric, but hidden symmetric, unit cells are depicted in Fig. 1(b), while the overall structure of our proposed lattice is depicted in Fig. 1(a). We emphasize that the unit cells shown in Fig. 1(b) are only two out of many possible ones. We shall discuss the systematic generation of large families of such

---

*These authors contributed equally to this work.
†Contact author: malte.rontgen@univ-lemans.fr
‡Contact author: wgao@eitech.edu.cn
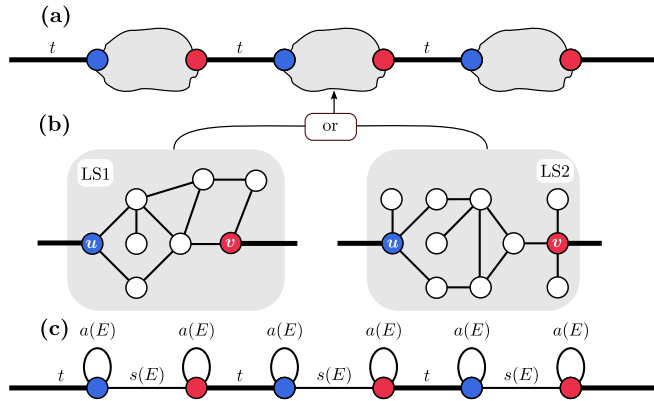§Contact author: coutant@lma.cnrs-mrs.fr

FIG. 1. Design of a latent SSH model. (a) The starting point: a one-dimensional lattice, with a cloud denoting a latently reflection symmetric subsystem. (b) Two unit cells LS1 and LS2. In both unit cells, the blue (u) and red (v) site are latently reflection symmetric. (c) Using a latently symmetric structure as a unit cell yields a latent SSH model. In all subfigures, each line corresponds to a coupling (with corresponding strength denoted, for instance, by t). Lines without annotations correspond to a coupling strength of unity. Loops denote on-site potentials. The sole purpose of (white, blue, red) colors is to highlight certain sites over others.

latently symmetric unit cells later on and show a couple of other examples in Appendix B.

Let us now build a lattice by choosing either LS1 or LS2 as a unit cell. We denote the Hamiltonian of our lattice by H; its eigenvalues and eigenstates can be obtained from solving the linear eigenvalue problem $H\Psi = E\Psi$. To uncover the hidden symmetry of the system, we will perform a so-called isospectral reduction, which is akin to an effective Hamiltonian [24]. To perform this reduction, one has to partition the system into two sets: S and its complement $\overline{S}$. For our problem, we will choose S to be all the blue and red sites in Fig. 1(b), while $\overline{S}$ will be all the white sites. The isospectral reduction

$$\widetilde{H}_S(E) = H_{SS} + H_{S\overline{S}}(E\,I - H_{\overline{S}\,\overline{S}})^{-1}H_{\overline{S}S}, \qquad (1)$$

with I the identity matrix, then converts our linear eigenvalue problem $H\Psi = E\Psi$ into the reduced, nonlinear problem

$$\widetilde{H}_S(E)\,\Psi_S = E\,\Psi_S. \qquad (2)$$

Here, Ψ_S denotes the S components of Ψ. We note that, in general, the original Hamiltonian and $\widetilde{H}_S(E)$ possess the same eigenvalue spectrum,[1] which motivates calling $\widetilde{H}_S(E)$ an isospectral reduction; see chapter 1 of Ref. [25]. We further note that the isospectral reduction could be interpreted as a tool that sheds light only on a fraction of sites (S), while leaving the remaining sites ($\overline{S}$) in darkness. In this sense, it provides a stroboscopic point of view on the system.

The isospectral reduction of our lattice is shown in pictorial form in Fig. 1(c). Taking the Fourier transform of the resulting

system, Eq. (2) is transformed to

$$\widetilde{H}_S^{(B)}(E, k)\,\Psi_S(k) = E\,\Psi_S(k) \qquad (3)$$

with the effective Bloch Hamiltonian

$$\widetilde{H}_S^{(B)}(E, k) = \begin{pmatrix} a(E) & s(E) + t\,e^{ik} \\ s(E) + t\,e^{-ik} & a(E) \end{pmatrix}. \qquad (4)$$

The crucial thing about $\widetilde{H}_S^{(B)}$ is the equality of its two diagonal elements $a(E)$. This equality is entirely due to a so-called latent reflection symmetry [15] of our unit cells LS1 and LS2. The name stems from the following observation: If one would take the isospectral reduction of the isolated unit cell (which is asymmetric) over $S = \{u, v\}$ (blue and red site), one would obtain a reflection-symmetric dimer. Thus, while the original unit cell is asymmetric, it indeed hosts a hidden reflection symmetry that is uncovered using the isospectral reduction. For this reason, we say that the unit cell hosts a latent reflection symmetry.

Let us note that the equality of the diagonal elements in $\widetilde{H}_S^{(B)}(E, k)$ would also occur if our unit cells would be reflection symmetric. For a generic unit cell which is neither reflection symmetric nor latently symmetric,[2] however, the two diagonal elements are generically unequal, though they may coincide for some specific values of E.

Due to the equality of the diagonal elements, we can rewrite Eq. (4) as

$$\begin{pmatrix} 0 & s(E) + te^{ik} \\ s(E) + te^{-ik} & 0 \end{pmatrix}\Psi_S(k) = \epsilon\,\Psi_S(k), \qquad (5)$$

with $\epsilon = E - a(E)$. This takes formally the mathematical form of the classical SSH model, though with energy-dependent intercell coupling $s(E)$ and energy-dependent eigenvalue $\epsilon(E)$. We thus see that the isospectral reduction of our initial system mimics the SSH model; this justifies calling the initial system a latent SSH model.

The algebraic mapping Eq. (5) between the classic SSH model and our latent SSH model is the key to understand the properties of the latter. The original SSH model has a topological transition at eigenvalue zero when $s = t$. In Eq. (5), an eigenvalue $\epsilon = 0$ only occurs when $E = a(E)$. Consequently, each solution E_i to $\epsilon(E) = 0$ corresponds to one topological transition, reached when the intercell coupling $|t| = |s(E_i)|$. Thus, the system is in the ith topological phase when the intercell coupling t fulfills $|t| > |s(E_i)|$. In a semi-infinite system, the ith topological phase displays edge states whose amplitudes on the sites u_n and v_n in the n-unit cell are $\Psi_{u_n} = (-\frac{s(E_i)}{t})^n$ and $\Psi_{v_n} = 0$.[3] We remark that the amplitudes on the remaining sites [the white ones, see Fig. 1(b)] of each unit cell can be obtained through $\Psi_{\overline{S}} = (H_{\overline{S}\,\overline{S}} - EI)^{-1}H_{\overline{S}S}\Psi_S$ and are, in particular, exponentially localized as well. Let us now apply the above to a concrete setup. In Fig. 2, we investigate the

---

[1]The eigenvalue spectrum of $\tilde{H}_S(E)$ is defined as the solutions to $\det(\tilde{H}_S(E) - EI)$.

---

[2]Or when choosing S such that it does not include sites which are related/mapped to each other by either a classical or a latent reflection symmetry.

[3]This expression follows by analogy from the corresponding expression of the classic SSH model which can be found in chapter 1.5.6. of Ref. [2].
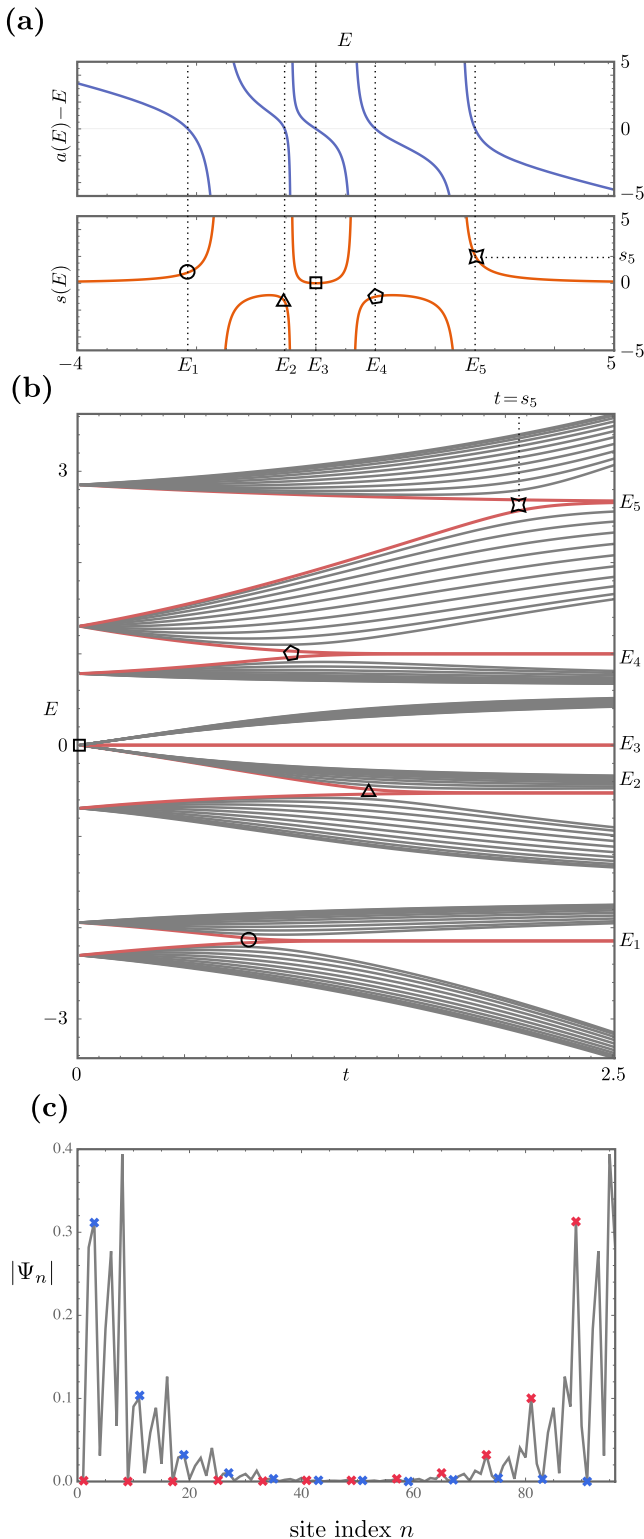
(a)

(b)

(c)

FIG. 2. Topological transitions of a latent SSH model. (a) The two curves $s(E)$ and $a(E) - E$ (see text for details), with the five topological transitions—occurring at energies E_1 to E_5—marked by different geometrical shapes. (b) The energy spectrum for a finite setup of $N = 12$ unit cells in dependence of the intercell coupling t, with topological transitions marked by the same shapes as in (a). (c) The spatial profile of one of the two edge states at energy E_1 for $t = 2.5$. Red/blue crosses denote the amplitude at sites u, v. For all cases, the lattice was built by using LS1 from Fig. 1(b) as a unit cell.

topological transitions for a setup with the eight-site unit cell LS1 displayed in Fig. 1(b). In particular, in Fig. 2(a), we show the two curves $a(E) - E$ and $s(E)$. As can be seen, there are five topological transitions. In Fig. 2(b), we show the energy eigenvalues for a finite setup of $N = 12$ unit cells (with eight sites per unit cell) for varying intercell coupling t. We clearly see that each transition is accompanied by the appearance of a pair of topological edge states that are exponentially localized on the left or the right end of the chain, as is illustrated in Fig. 2(c) for one of the states.

Regarding the edge states of latent SSH models, two things are noteworthy. First, by using the latent symmetry of sites u and v, the existence of these states can further be related to a quantized Zak phase of both the reduced and the unreduced system, as we show in Appendix D. Second, it is well known that the edge states of the conventional SSH lattice are robust with respect to disorder that respects chiral symmetry. Here, since the intercell coupling t is independent of the energy, this robustness with respect to disorder in t is—due to Eq. (5)—inherited by a latent SSH model as well.

Before we continue, we remark that the presence of topological edge states in latently symmetric systems is not limited to latent SSH models, as has very recently been demonstrated in the context of granular media [26].

B. Robustness with respect to orientational disorder

Besides the aforementioned robustness that it inherits from the classic SSH model, a latent SSH model furthermore features a new kind of robustness with respect to what we call here "orientational disorder." Such disorder emerges if one changes the orientation—that is, performing a rotation of $180°$, which in particular exchanges u and v—of one or more unit cells. In Appendix C, we show an example realization of this disorder. Remarkably, the isospectral reduction of the system is completely unaffected by orientational disorder. As a consequence, topological transitions, the emergence of edge states, and even the band structure of the system are all retained, even if the translational invariance of the full system is broken by orientational disorder.

C. Construction principles

A crucial ingredient to construct latent SSH models is latently symmetric unit cells, which can be easily designed using graph theoretical techniques [27]. Alternatively, even when restricting oneself to systems with less than 12 sites and all unit couplings, one can easily generate several million latently symmetric setups through an exhaustive search. More specifically, using the NAUTY suite [28], one can efficiently construct all setups with a given number of sites, and then test each setup for a latent symmetry by scanning the first few matrix powers of each setup [29]. We emphasize that latently symmetric systems are rather robust. That is, they can be altered in certain ways (changing certain couplings and/or on-site potentials) without breaking latent symmetry [29,30]. For instance, as long as the on-site potentials of two latently symmetric sites remain identical, they can be set to any value. In Appendix B we show a couple of such changes of the unit cell LS2 while maintaining its latent symmetries.
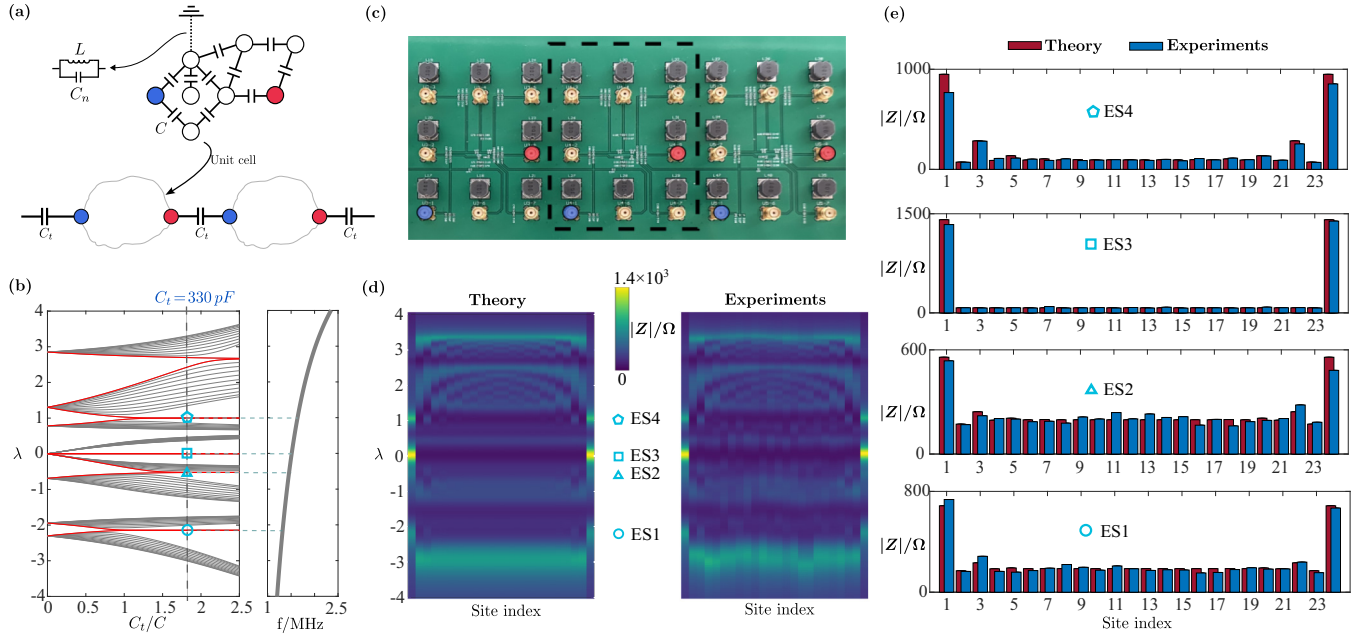
FIG. 3. Circuit realization of a latent SSH model. (a) Schematic of the latent topological circuit and its unit cell. Each site n is grounded through a capacitor C_n in parallel to an inductor L, though we depict this grounding only for one site to keep the figure as clear as possible. (b) Resonance frequency dispersion of a finite 12-unit-cell circuit in dependence of C_t. The topological edge states visible at $C_t = 330$ pF are marked by four different geometrical shapes which are used in (d) and (e) as well. (c) Photograph showing three unit cells of the printed circuit. (d) Theoretical and experimental impedance value across all the latently symmetric points. (e) Impedance profile across the latently symmetric points at various frequencies that correspond to the topological edge states.

D. Number of topological phases

An important property of a latent SSH model is that it can possess not only one but multiple topologically protected edge modes. The number of these modes is equivalent to the number of solutions to $a(E) = E$. Using the definition of the isospectral reduction, Eq. (1), it can be shown that $a(E) = p(E)/q(E)$ is a rational function in E, with the degree $\deg(p) < \deg(q) \leqslant N - 2$, where N is the number of sites in the unit cell. The number of topological phases is then given by the degree of the numerator of $a(E) - E = \frac{p(E)-Eq(E)}{q(E)}$. It follows that a latent SSH model has at least 1 and at most $N - 1$ topological phases.

III. EXPERIMENTAL REALIZATION

In the following, we implement a latent SSH model with electrical circuits. We first review the theoretical description of the setup, which is depicted in Fig. 3(a). Here, each site (vertex) of the original eight-site setup of Fig. 1(b) has been replaced by a junction, and each coupling (edge) by a capacitor. Additionally, each site n is now grounded through an inductance L parallel to a capacitance $C_n = 5C - \Sigma_n$, where Σ_n is the total capacitance of capacitors connecting site n to other sites. To link the electric circuit to the latent SSH model, we go to an eigenmode analysis. Starting from Kirchhoff's and Ohm's laws in the frequency domain, it can be shown that the eigenmodes $\mathbf{V}$ (whose entries describe the voltages at the junctions) and eigenfrequencies ω of the circuit are obtained by solving the eigenvalue problem (see Appendix E for details)

$$H_P \mathbf{V} = \lambda \mathbf{V}, \tag{6}$$

where H_P is the tight-binding Hamiltonian of the eight-site unit cell LS1 of Fig. 1(b), and $\lambda = \frac{L\omega^2(5C+C_t)-1}{LC\omega^2}$.

In order to test the predictions of the theory, we measured the circuit eigenmodes and eigenfrequencies, that is, their resonances. In circuit systems, these generally manifest themselves as peaks in the impedance spectrum, which can be conveniently measured [7,31–38]. To see this, let us investigate the single-port impedance $Z_{a,a}$ of port a. This impedance can be obtained by connecting a cable to port a, applying a voltage V_a and measuring the current I_a into/out of this port; all other ports are not connected to external cables. Using Kirchhoff's and Ohm's law and some algebra, we see that $Z_{a,a}$ can be expanded in terms of the eigenvalues λ_n and eigenvectors $\mathbf{V}^{(n)}$ of H_P as

$$Z_{a,a}(\omega) = \frac{V_a}{I_a} = \frac{i}{\omega C}\left(\frac{1}{H_P - \lambda}\right)_{a,a} = \frac{i}{\omega C}\sum_n \frac{|V_a^{(n)}|^2}{\lambda_n - \lambda}. \tag{7}$$

At resonance, that is, when the frequency ω is chosen such that $\lambda(\omega_R) \approx \lambda_n(\omega_R)$, the sum is dominated by the nth term, and $Z_{a,a}(\omega_R)$ yields the spatial profile of $|\mathbf{V}^{(n)}|^2$. We can thus determine *both* the eigenfrequencies and eigenmodes of the circuit by measuring the frequency-dependent single-port impedances along the circuit.

For our experiments, we fabricated a circuit comprising 12 unit cells using standard printed circuit board (PCB) technique (sample details are provided in Methods). A snapshot of three unit cells used in our experiments is given in Fig. 3(c). Low loss wire wound inductors (CY105-100K) are used, whose nominal inductance is 10 μH with 10% tolerance. However, our measurements show that the actual inductance is

approximately 9 μH, with a parasitic resistance around 2 Ω at the frequency range of interest; see Appendix E. Unless otherwise mentioned, the theoretical calculations are performed with these values. To allow for the impedance measurements, each node in our circuit is connected to a SMA port [see Fig. 3(c)]. Utilizing a vector network analyzer (R&S ZNL3) [39,40], we first measured the circuit single-port scattering parameters $S(\omega)$, and subsequently converted them to impedance by $Z = Z_0 \frac{1-S}{1+S}$, with $Z_0 = 50$ Ω being the characteristic impedance of the microwave cable.

In Fig. 3(b), we show a theoretical computation of the eigenfrequency spectrum of our circuit in dependence of the intercell capacitance C_t, with 9-μH grounding inductances but without parasitic resistance according to Eq. (6). Solid red lines represent the localized edge states.[4] For our experiments shown in the following, we have chosen $C_t = 330$ pF, for which the setup has four (out of the five possible) topological edge state pairs. Further experimental results for $C_t = 820$ pF, where all five topological edge state pairs are visible, are illustrated in Appendix E. In Fig. 3(d), we show both the theoretical computation and the measured values of the single-port impedance Z. Both quantities are shown as a two-dimensional color map, with the free parameters being the operating frequency and site number. Topological edge states are found at the four frequencies ES1 to ES4, with the corresponding impedance measurements being shown in more detail in Fig. 3(e). Overall, our experiments are in excellent agreement with the theory. We note that the deviation in localization behavior from the idealized situation (exponential decay) is due to the non-negligible parasite resistance of inductors, which is included in our theoretical calculations.

IV. CONCLUSIONS

Let us now put our paper and its perspectives in a greater context. In a nutshell, the proposed latent SSH models are the result of an augmentation principle that combines the richness of a graph with the topological nature of the SSH model.

As a consequence, latent SSH models inherit the emergence of topological edge states, but are augmented by having many more than just a single topological transition. On a technical level, this augmentation was done by choosing an oversized original system with no apparent symmetries and then replacing it by another one through isospectral reduction; it actually provides a stroboscopic point of view on the system, making to appear symmetries that were hidden.

It is thus clear that our augmentation principle is not limited to the SSH model, but can be applied to a plethora of other systems. This includes non-Hermitian systems such as the iconic Hatano-Nelson model, of which we have very recently designed a latent version [41].

Overall, both the latent SSH model proposed here as well the underlying augmentation principle offer various interesting perspectives. The immediate next steps would be the design of latent versions of slightly more complex systems

such as graphene or the Haldane model. Moreover, we foresee experimental realizations of our latent SSH model in other platforms such as acoustic or microwave waveguide networks.

APPENDIX A: SAMPLE FABRICATION DETAILS

We fabricated a double layer PCB comprising 12 unit cells using LCEDA program software. The substrate material is FR4 with a 1-oz copper layer on both top and bottom layers. Ground planes are poured on both the top and bottom layer to create a solid, low-impedance path for return currents. Low loss wire wound inductors (CY105-100K) are used to connect all the nodes to the mutual ground, whose nominal inductance is 10 μH with 10% tolerance. For the 180-pF capacitors that are used for inner-cell couplings and the 330- and 180-pF capacitors for intercell couplings, we use SMD ceramic capacitors provided by Murata (serial numbers GRM0335C1E181FA01, GRM0335C1E331FA01, and GRM0335C1E821FA01).

APPENDIX B: MORE EXAMPLES OF LATENTLY SYMMETRIC SETUPS

In the main text, we mentioned that one can easily generate a plethora of latently symmetric unit cells by relying on graph-theoretical tools. Figures 5(b)–5(d) show three example systems that have been obtained with this method. We further mentioned that one can analyze the matrix powers of a given latently symmetric setup to derive changes to the system that preserve its latent symmetry. In Fig. 5(e), we visualize the outcome of this approach—whose derivation can be found in Ref. [30]—for the unit cell LS2 from Fig. 1(b) of the main text. The latent symmetry of sites u and v is preserved for any choice of the real coupling strengths a, b, c, d, e, and f. Moreover, one may freely and individually vary the on-site potentials of sites x, y, and z, and—though by keeping these two identical—the on-site potentials of sites u and v.

APPENDIX C: EXAMPLE REALIZATION OF ORIENTATIONAL DISORDER

Figure 4 shows a finite section of a latent SSH chain that features orientational disorder. The orientation-changing of individual unit cells is obtained by rotating them by 180° and is additionally indicated by denoting the unit cell as ˥ꙄꙆ instead of LS1. As written in the main text, the isospectral reduction of such an orientationally disordered system is the same as that of the nondisordered one.

APPENDIX D: QUANTIZATION OF THE ZAK PHASE DUE TO LATENT SYMMETRY

In the following, we show that a latent SSH model features a quantized Zak phase. To this end, let us start by assuming that our unit cell Hamiltonian is real valued and with two latently symmetric sites u and v, like the one depicted in Fig. 5.

---

[4]Note that the latently symmetric sites at the very boundary require an extra C_t grounding capacitor for faithfully corresponding to the tight-binding model; see Appendix E.
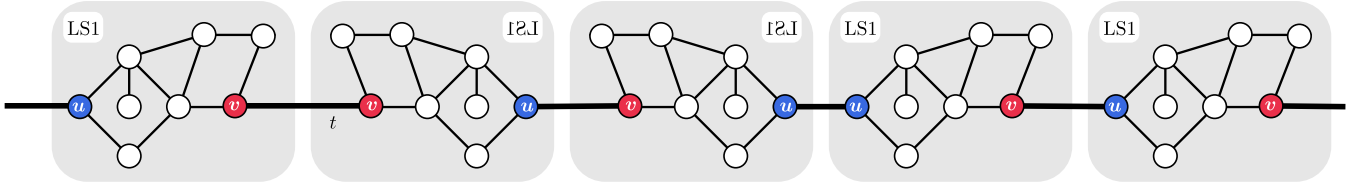
FIG. 4. A part of an orientationally disordered latent SSH chain.

To be explicit, let us choose the setup depicted in Fig. 5(a), whose Hamiltonian reads

$$H = h \begin{pmatrix} 0 & 0 & \sqrt{2} & 0 \\ 0 & 0 & 1 & 1 \\ \sqrt{2} & 1 & 0 & 0 \\ 0 & 1 & 0 & 0 \end{pmatrix}. \quad \text{(D1)}$$

Now, whenever we have such a real-valued latently symmetric Hamiltonian, there exists a block-diagonal matrix (numbering the sites such that $S = \{u, v\}$ are the first two)

$$Q = \begin{pmatrix} 0 & 1 & \\ 1 & 0 & \\ & & \overline{Q} \end{pmatrix} \quad \text{(D2)}$$

which (i) commutes with H; (ii) is symmetric, that is, $Q = Q^T$; and (iii) is orthogonal, $Q^T = Q^{-1}$ (see Lemma 11.1 in Ref. [43],[5] or Sec. IV of the Supplemental Material of Ref. [18]), from which it follows that $Q^2 = I$. In other words, Q acts as a permutation on the two sites S, while it acts as an orthogonal transformation $\overline{Q}$ on the sites $\overline{S}$. For our example of Fig. 5, we have

$$Q = \begin{pmatrix} 0 & 1 & 0 & 0 \\ 1 & 0 & 0 & 0 \\ 0 & 0 & \frac{1}{\sqrt{2}} & \frac{1}{\sqrt{2}} \\ 0 & 0 & \frac{1}{\sqrt{2}} & -\frac{1}{\sqrt{2}} \end{pmatrix}. \quad \text{(D3)}$$

Now, when we use our latently symmetric Hamiltonian H as a unit cell and build a lattice by connecting sites u and v of

---

[5]In this lemma, the phrasing "latently symmetric" is not used; instead, the two sites u and v are said to be cospectral. For a real-symmetric matrix H, cospectrality of two sites u and v, and the statement that they are latently symmetric are equivalent, see Ref. [42].
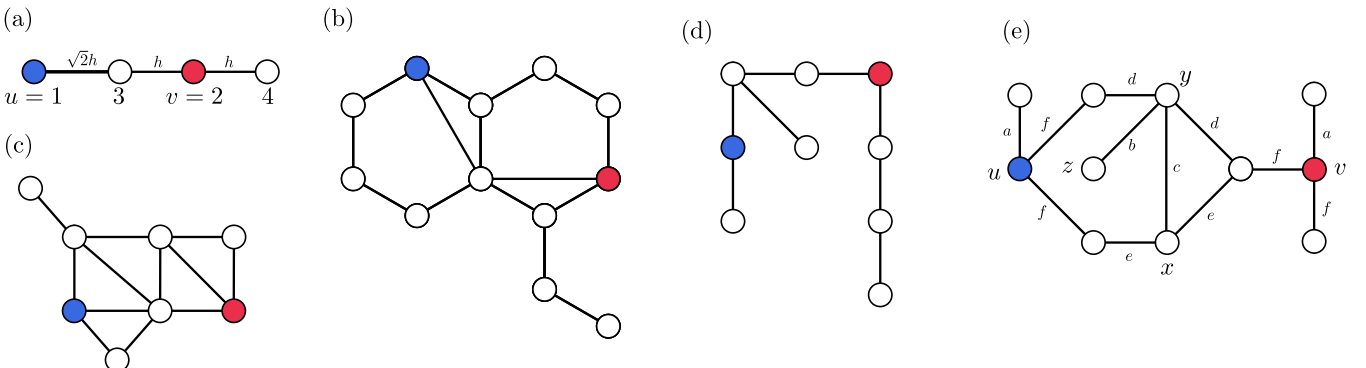
neighboring unit cells, our Bloch Hamiltonian $H_B(k)$ fulfills

$$Q H_B(k) Q = H_B(-k). \quad \text{(D4)}$$

This means in particular that if $\varphi_n(k)$ is an eigenvector for $H_B(k)$, $Q\varphi_n(k)$ is an eigenvector for $H_B(-k)$ with the same eigenvalue. Because we assume the eigenvalues to be all non-degenerate (nonoverlapping bands) this means

$$\varphi_n(-k) = e^{i\theta(k)} Q \varphi_n(k), \quad \text{(D5)}$$

where $\theta(k)$ is a locally smooth function of k. In particular, on the band edges, $k = 0$ or π are mirror symmetric momenta (since $k = -\pi$ is equivalent to $k = \pi$). At these values of k, Q commutes with the Hamiltonian, and hence, φ_n is either symmetric or antisymmetric, i.e., $\theta(0)$ and $\theta(\pi)$ are either zero or π.

If $\varphi_n(q)$ is the Bloch eigenvector of the nth band, we define the Berry connection [2]

$$A_n(k) = -i \langle \varphi_n | \partial_k \varphi_n \rangle. \quad \text{(D6)}$$

The Zak phase is defined as the integral of the Berry connection over the Brillouin zone:

$$\alpha_Z = \oint_{-\pi}^{\pi} A_n(k) dk. \quad \text{(D7)}$$

The mirror symmetry commutation relation with the Hamiltonian in Eq. (D4) gives us a relation between the Berry connection at k and $-k$. After taking the derivative of Eq. (D4) and taking the scalar product with $\varphi_n(-k)$, we see that

$$A_n(-k) = A_n(k) + \partial_q \theta. \quad \text{(D8)}$$

In other words, the Berry connection at k differs from that at $-k$ by a gauge. Now, if we integrate that relation over half of the Brillouin zone, we obtain

$$-\int_{-\pi}^{0} A_n(k) dq = \int_{0}^{\pi} A_n(k) dq + \theta(\pi) - \theta(0). \quad \text{(D9)}$$

FIG. 5. Five latently symmetric systems (see text for details). Unless otherwise marked, all couplings are equal to unity.
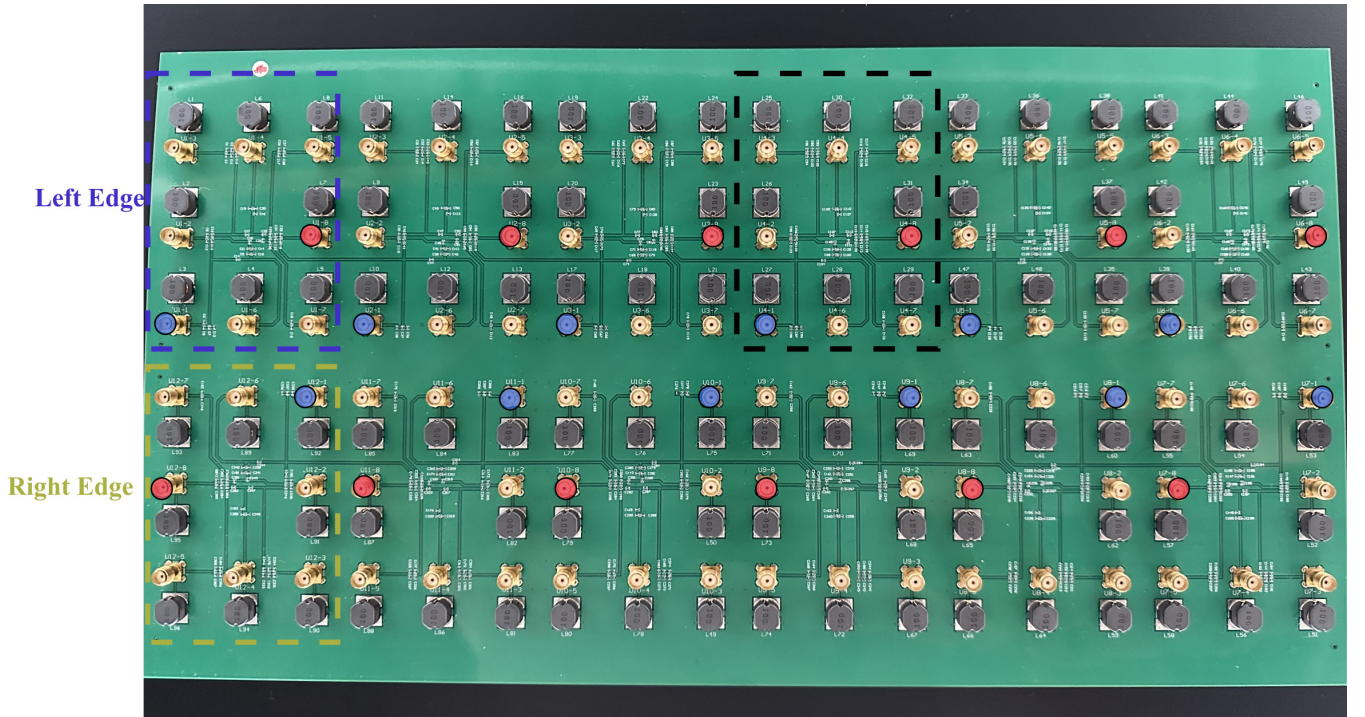
FIG. 6. Snapshot of the full 12-unit-cell latent SSH circuit.

Combining the two integrals gives the integral over the whole Brillouin zone, and hence, the Zak phase. The latter then has the simple expression

$$\alpha_Z = \theta(\pi) - \theta(0), \tag{D10}$$

from which it follows that either $\alpha_Z = 0 \mod 2\pi$ (both edge eigenvectors have the same symmetry) or $\alpha_Z = \pi \mod 2\pi$ (the two eigenvectors do not have the same symmetry).

We note that one could repeat the above steps for the effective Hamiltonian as well. The starting point would then not be Eq. (D4), but

$$M\widetilde{H}_S^{(B)}(E, k)M = \widetilde{H}_S^{(B)}(E, k), \tag{D11}$$

with $M = \begin{pmatrix} 0 & 1 \\ 1 & 0 \end{pmatrix}$ and with $\widetilde{H}_S^{(B)}(E, k)$ given by Eq. (4), that is,

$$\widetilde{H}_S^{(B)}(E, k) = \begin{pmatrix} a(E) & s(E) + t\, e^{ik} \\ s(E) + t\, e^{-ik} & a(E) \end{pmatrix}. \tag{D12}$$
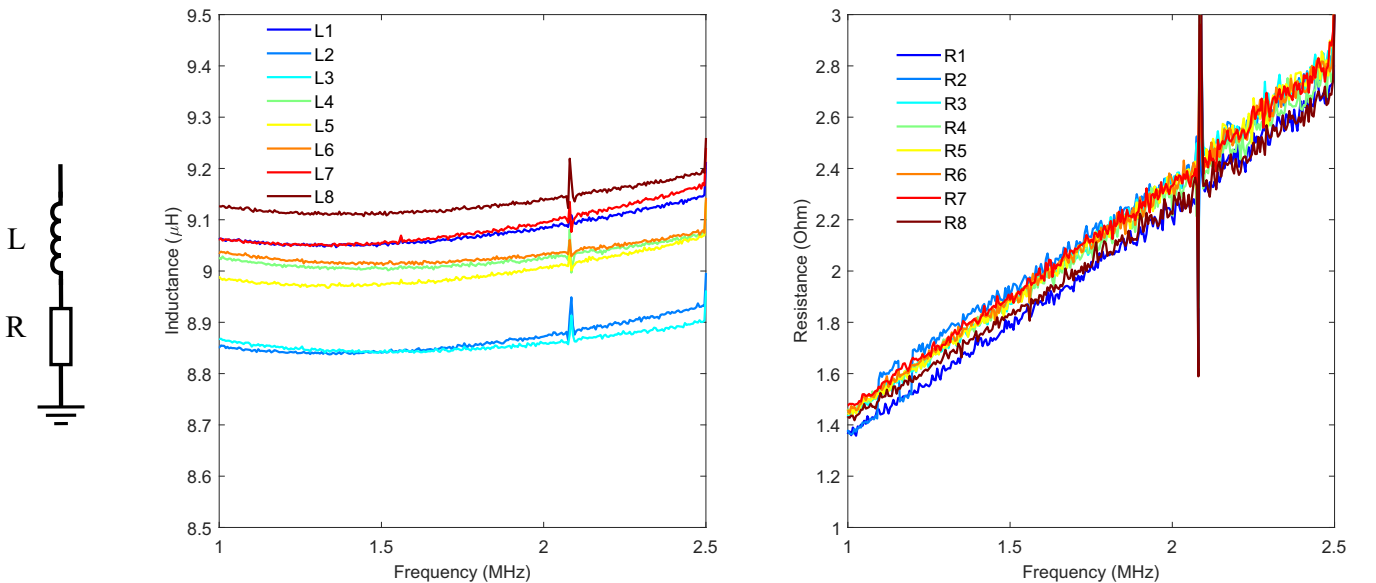

FIG. 7. Experimentally measured inductance and the parasitic resistance of the inductors utilized in the latent SSH circuit.
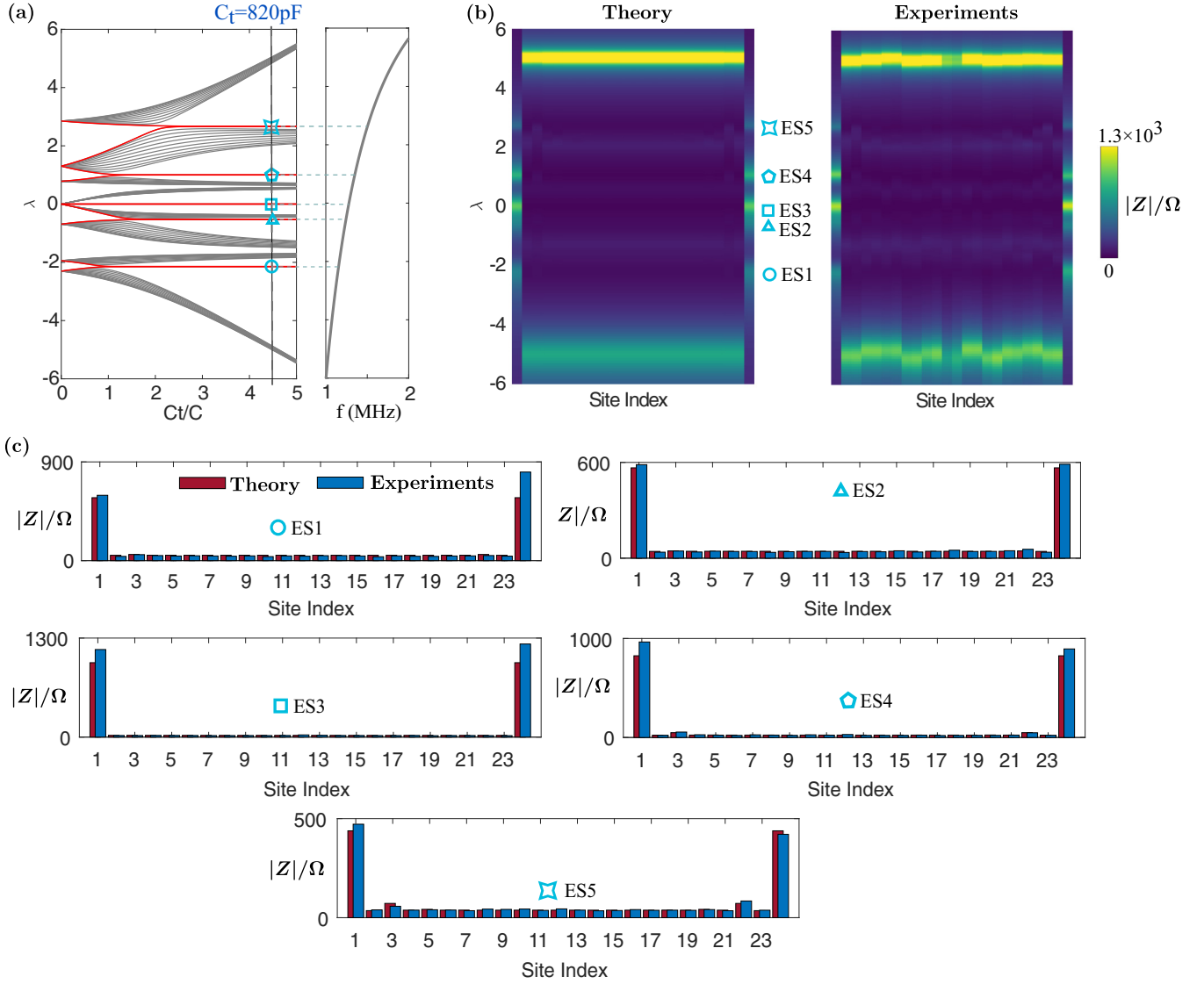
FIG. 8. (a) Resonance frequency dispersion of a finite 12-unit-cell circuit in dependence of C_t. The topological edge states visible at $C_t = 820$ pF are marked by five different geometrical shapes which are used in (b) and (c) as well. (b) Theoretical and experimental impedance value across all the latently symmetric points. (c) Impedance profile across the latently symmetric points at various frequencies that correspond to the topological edge states.

Based on Eq. (D11), the steps of Eqs. (D5)–(D10) can all be repeated, resulting in a quantized Zak phase of the effective model.

APPENDIX E: DETAILS REGARDING THE EXPERIMENTAL SETUP

Before going into details, let us start by providing a snapshot of the full 12-unit-cell latent SSH circuits; see Fig. 6. The latently symmetric points are marked by blue/red circles. Unit cells 6 to 12 are folded back to keep the circuit compact. Leftmost and rightmost cells are highlighted by blue and yellow dashed lines, respectively. Cospectral sites are highlighted by blue and red full circles, as they are in Fig. 3(b) of the main text.

1. Deriving the linear eigenvalue problem and the impedance formula

In the following, we shall derive the linear eigenvalue problem Eq. (6) of the main text, that is,

$$H_P \mathbf{V} = \lambda \mathbf{V}. \qquad (E1)$$

To do so, we assume that each node/site of the circuit is connected via an extra cable to the exterior, so that current can flow into/out of the circuit. Denoting by $\mathbf{V}$ the voltage at the current's nodes, and by $\mathbf{I}$ the current flowing into/out of the nodes, we can use Kirchhoff's and Ohm's law in frequency space to derive the important relation

$$J(\omega)\mathbf{V} = \mathbf{I}. \qquad (E2)$$

Here, $J(\omega) = -i\omega C H_P + i\omega(5C + C_t)I + \frac{1}{i\omega L}I$ is the so-called circuit Laplacian [7] with H_P the tight-binding

Hamiltonian of the eight-site model of Fig. 1(b) of the main text. Eigenmodes occur when there is no external current flowing into the circuit, that is, $\mathbf{I} = 0$, and we obtain the quadratic eigenvalue problem

$$J(\omega)\mathbf{V} = 0. \tag{E3}$$

Since the second and third term of J are proportional to the identity matrix, Eq. (E3) can be written as the linear eigenvalue problem $H\mathbf{V} = \frac{1}{\omega^2}\mathbf{V}$ with $H = L((5C + C_t)I - CH_P)$. Equation 6 is then a direct consequence. We note that we also have

$$J(\omega) = -i\omega C(H_P - \lambda). \tag{E4}$$

When calculating the single-port impedance

$$Z_{a,a}(\omega) = \frac{V_a}{I_a} = \frac{i}{\omega C}\left(\frac{1}{H_P - \lambda}\right)_{a,a} = \frac{i}{\omega C}\sum_n \frac{\left|V_a^{(n)}\right|^2}{\lambda_n - \lambda} \tag{E5}$$

[Eq. (7)], the relations Eqs. (E2) and (E4) can be used to express

$$Z_{a,a}(\omega) = \frac{V_a}{I_a} = (J^{-1})_{a,a} = \frac{i}{\omega C}[(H_P - \lambda)^{-1}]_{a,a}, \tag{E6}$$

which is the expression used in Eq. (7). When parasitic resistances R of the inductors are considered, the circuit Laplacian is modified as

$$J(\omega) = -i\omega CH_P + i\omega(5C + C_t)I + \frac{1}{i\omega L + R}I \tag{E7}$$

in which R is the parasitic serial resistance of the inductors (see below) and can be subsequently implemented for the single-port impedance calculations. Accordingly under parasitic resistance, Eq. (7) can be modified as

$$Z_{a,a}(\omega) = \frac{i}{\omega C}\sum_n \frac{\left|V_a^{(n)}\right|^2}{\lambda_n - \lambda + \eta},$$
$$\eta = -\frac{1}{\omega^2 LC}\frac{R}{R + i\omega L}. \tag{E8}$$

2. Inductance/parasite resistance measurements

In the following, we show the experimentally measured inductance and parasite resistance of the inductors. The results are given in Fig. 7. To do so, we unsolder all the grounding and coupling capacitors of the circuit and measure impedance of grounding inductors only. The impedance value is then converted to inductance and resistance for each frequency, assuming they are serially connected; see Fig. 7. We found that the inductance is lower than the nominal value of 10 μH and is close to 9 μH. The parasite resistance dispersed almost linearly from 1.4 to 2.8 Ω, which are significantly larger than the nominal DC resistance, 0.034 Ω, probably due to skin effect induced extra loss at higher frequencies. Here we omit discussing the detailed parasite effects in such surface-mounted components that introduce dispersed inductance and resistance rather than constants, and adopting constant values that are close to experiments in our theoretical model, granted such means have already provided accurate predictions and are consistent with experimental results.

3. Experiments with $C_t = 820$ pF

In Fig. 8, we show the comparisons of experimental and theoretical results with $C_t = 820$ pF, for which the setup has five topological edge state pairs. In Fig. 8(a), we show a theoretical computation of the eigenfrequency spectrum of our circuit in dependence of the intercell capacitance C_t, with 9-μH grounding inductances but without parasitic resistance, same as Fig. 3 of the main text. Solid red lines represent the localized edge states. In Fig. 8(b), we show both the theoretical computation and the measured values of the single-port impedance Z. Both quantities are shown as a two-dimensional color map, with the free parameters being the operating frequency and site number. Topological edge states are found at the five frequencies ES1 to ES5, with the corresponding impedance measurements being shown in more detail in Fig. 8(c). Overall, since the chosen coupling capacitance $C_t = 820$ pF is located deep in the topological region, localization of the edge states is stronger than in Fig. 3 of the main text.

[1] W. P. Su, J. R. Schrieffer, and A. J. Heeger, Solitons in polyacetylene, Phys. Rev. Lett. **42**, 1698 (1979).

[2] J. K. Asbóth, L. Oroszlány, and A. Pályi, *A Short Course on Topological Insulators: Band Structure and Edge States in One and Two Dimension*, 1st ed., Lecture Notes in Physics (Springer, New York, 2016), Vol. 919.

[3] Z.-G. Chen, L. Wang, G. Zhang, and G. Ma, Chiral symmetry breaking of tight-binding models in coupled acoustic-cavity systems, Phys. Rev. Appl. **14**, 024023 (2020).

[4] A. Coutant, A. Sivadon, L. Zheng, V. Achilleos, O. Richoux, G. Theocharis, and V. Pagneux, Acoustic Su-Schrieffer-Heeger lattice: Direct mapping of acoustic waveguides to the Su-Schrieffer-Heeger model, Phys. Rev. B **103**, 224309 (2021).

[5] M. Kremer, L. J. Maczewsky, M. Heinrich, and A. Szameit, Topological effects in integrated photonic waveguide structures, Opt. Mater. Express **11**, 1014 (2021).

[6] T. Tian, Y. Ke, L. Zhang, S. Lin, Z. Shi, P. Huang, C. Lee, and J. Du, Observation of dynamical phase transitions in a topological nanomechanical system, Phys. Rev. B **100**, 024310 (2019).

[7] C. H. Lee, S. Imhof, C. Berger, F. Bayer, J. Brehm, L. W. Molenkamp, T. Kiessling, and R. Thomale, Topolectrical circuits, Commun. Phys. **1**, 39 (2018).

[8] H. Guo and S. Chen, Kaleidoscope of symmetry-protected topological phases in one-dimensional periodically modulated lattices, Phys. Rev. B **91**, 041402(R) (2015).

[9] A. Anastasiadis, G. Styliaris, R. Chaunsali, G. Theocharis, and F. K. Diakonos, Bulk-edge correspondence in the trimer Su-Schrieffer-Heeger model, Phys. Rev. B **106**, 085109 (2022).

[10] D. Xie, W. Gou, T. Xiao, B. Gadway, and B. Yan, Topological characterizations of an extended Su-Schrieffer-Heeger model, npj Quantum Inf. **5**, 55 (2019).

[11] B. Pérez-González, M. Bello, Á. Gómez-León, and G. Platero, Interplay between long-range hopping and disorder in topological systems, Phys. Rev. B **99**, 035146 (2019).

[12] S. Biswas, A. Mukherjee, and A. Chakrabarti, Flat bands, edge states and possible topological phases in a branching fractal, arXiv:2209.05117.

[13] F. Liu and K. Wakabayashi, Novel topological phase with a zero Berry curvature, Phys. Rev. Lett. **118**, 076803 (2017).

[14] F. Liu, Analytic solution of the *n*-dimensional Su-Schrieffer-Heeger model, Phys. Rev. B **108**, 245140 (2023).

[15] D. Smith and B. Webb, Hidden symmetries in real and theoretical networks, Physica A **514**, 855 (2019).

[16] C. V. Morfonios, M. Röntgen, M. Pyzh, and P. Schmelcher, Flat bands by latent symmetry, Phys. Rev. B **104**, 035105 (2021).

[17] D. Leykam, A. Andreanov, and S. Flach, Artificial flat band systems: from lattice models to experiments, Adv. Phys. **3**, 1473052 (2018).

[18] M. Röntgen, M. Pyzh, C. V. Morfonios, N. E. Palaiodimopoulos, F. K. Diakonos, and P. Schmelcher, Latent symmetry induced degeneracies, Phys. Rev. Lett. **126**, 180601 (2021).

[19] M. Röntgen, C. V. Morfonios, P. Schmelcher, and V. Pagneux, Hidden symmetries in acoustic wave systems, Phys. Rev. Lett. **130**, 077201 (2023).

[20] J. Sol, M. Röntgen, and P. del Hougne, Covert scattering control in metamaterials with non-locally encoded hidden symmetry, Adv. Mater. **36**, 2303891 (2024).

[21] M. Röntgen, O. Richoux, G. Theocharis, C. V. Morfonios, P. Schmelcher, P. del Hougne, and V. Achilleos, Equireflectionality and customized unbalanced coherent perfect absorption in asymmetric waveguide networks, Phys. Rev. Appl. **20**, 044082 (2023).

[22] X. Cui, R.-Y. Zhang, X. Wang, W. Wang, G. Ma, and C. T. Chan, Experimental realization of stable exceptional chains protected by non-Hermitian latent symmetries unique to mechanical systems, Phys. Rev. Lett. **131**, 237201 (2023).

[23] M. Röntgen, Latent symmetries: An introduction, MetaMAT Weekly Seminars, online talk (2022).

[24] G. Grosso and G. P. Parravicini, *Solid State Physics*, 2nd ed. (Academic, New York, 2014).

[25] L. Bunimovich and B. Webb, *Isospectral Transformations: A New Approach to Analyzing Multidimensional Systems and Networks*, 1st ed., Springer Monographs in Mathematics (Springer, New York, 2014).

[26] L.-Y. Zheng, Y.-F. Li, J. Zhang, and Y. Huang, Robust topological edge states induced by latent mirror symmetry, Phys. Rev. B **108**, L220303 (2023).

[27] C. D. Godsil and B. D. McKay, Constructing cospectral graphs, Aequ. Math. **25**, 257 (1982).

[28] B. D. McKay and A. Piperno, Practical graph isomorphism, II, J. Symb. Comput. **60**, 94 (2014).

[29] M. Röntgen, N. E. Palaiodimopoulos, C. V. Morfonios, I. Brouzos, M. Pyzh, F. K. Diakonos, and P. Schmelcher, Designing pretty good state transfer via isospectral reductions, Phys. Rev. A **101**, 042304 (2020).

[30] C. V. Morfonios, M. Pyzh, M. Röntgen, and P. Schmelcher, Cospectrality preserving graph modifications and eigenvector properties via walk equivalence of vertices, Linear Algebra Appl. **624**, 53 (2021).

[31] S. Imhof, C. Berger, F. Bayer, J. Brehm, L. W. Molenkamp, T. Kiessling, F. Schindler, C. H. Lee, M. Greiter, T. Neupert, and R. Thomale, Topolectrical-circuit realization of topological corner modes, Nat. Phys. **14**, 925 (2018).

[32] N. A. Olekhno, E. I. Kretov, A. A. Stepanenko, P. A. Ivanova, V. V. Yaroshenko, E. M. Puhtina, D. S. Filonov, B. Cappello, L. Matekovits, and M. A. Gorlach, Topological edge states of interacting photon pairs emulated in a topolectrical circuit, Nat. Commun. **11**, 1436 (2020).

[33] Y. Wang, H. M. Price, B. Zhang, and Y. D. Chong, Circuit implementation of a four-dimensional topological insulator, Nat. Commun. **11**, 2356 (2020).

[34] W. Zhang, F. Di, X. Zheng, H. Sun, and X. Zhang, Hyperbolic band topology with non-trivial second Chern numbers, Nat. Commun. **14**, 1083 (2023).

[35] H. Yang, L. Song, Y. Cao, and P. Yan, Realization of Wilson fermions in topolectrical circuits, Commun. Phys. **6**, 211 (2023).

[36] Z. Wang, X.-T. Zeng, Y. Biao, Z. Yan, and R. Yu, Realization of a Hopf insulator in circuit systems, Phys. Rev. Lett. **130**, 057201 (2023).

[37] L. Li, C. H. Lee, S. Mu, and J. Gong, Critical non-Hermitian skin effect, Nat. Commun. **11**, 5491 (2020).

[38] J. Wu, Z. Wang, Y. Biao, F. Fei, S. Zhang, Z. Yin, Y. Hu, Z. Song, T. Wu, F. Song, and R. Yu, Non-Abelian gauge fields in circuit systems, Nat. Electron. **5**, 635 (2022).

[39] S. Liu, S. Ma, Q. Zhang, L. Zhang, C. Yang, O. You, W. Gao, Y. Xiang, T. J. Cui, and S. Zhang, Octupole corner state in a three-dimensional topological circuit, Light Sci. Appl. **9**, 145 (2020).

[40] S. Liu, S. Ma, C. Yang, L. Zhang, W. Gao, Y. J. Xiang, T. J. Cui, and S. Zhang, Gain- and loss-induced topological insulating phase in a non-Hermitian electrical circuit, Phys. Rev. Appl. **13**, 014047 (2020).

[41] L. Eek, A. Moustaj, M. Röntgen, V. Pagneux, V. Achilleos, and C. M. Smith, Emergent non-Hermitian models, Phys. Rev. B **109**, 045122 (2024).

[42] M. Kempton, J. Sinkovic, D. Smith, and B. Webb, Characterizing cospectral vertices via isospectral reduction, Linear Algebra Appl. **594**, 226 (2020).

[43] C. Godsil and J. Smith, Strongly cospectral vertices, arXiv:1709.07975.